
Article:
Blackburn, L., Crawford, R., Walling, S. et al. (9 more authors) (2021) Influence of accessory phases and surrogate type on accelerated leaching of zirconolite wasteforms. npj Materials Degradation, 5. 24. ISSN 2397-2106

https://doi.org/10.1038/s41529-021-00171-8

---

npj | Materials Degradation

www.nature.com/npjmatdeg

ARTICLE OPEN

Check for updates

Influence of accessory phases and surrogate type on accelerated leaching of zirconolite wasteforms

Lewis R. Blackburn[1], Rachel Crawford[1], Samuel A. Walling[1], Laura J. Gardner[1], Max R. Cole[1], Shi-Kuan Sun[1], Clémence Gausse[1], Amber R. Mason[1], Martin C. Stennett[1], Ewan R. Maddrell[2], Neil C. Hyatt[1] and Claire L. Corkhill[1]✉

A fraction of the UK Pu inventory may be immobilised in a zirconolite ceramic matrix prior to disposal. Two zirconolite compositions, targeting $CaZr_{0.80}Ce_{0.20}Ti_2O_7$ and $CaZr_{0.80}U_{0.20}Ti_2O_7$, were fabricated by hot isostatic pressing, alongside a reformulated composition, nominally $Ca_{0.80}Zr_{0.90}Ce_{0.30}Ti_{1.60}Al_{0.40}O_7$, with an excess of Ti and Zr added to preclude the formation of an accessory perovskite phase. Materials were subjected to accelerated leaching in a variety of acidic and alkaline media at 90 °C, over a cumulative period of 14 d. The greatest Ce release was measured from $CaZr_{0.80}Ce_{0.20}Ti_{2.00}O_7$ exposed to 1 M H_2SO_4, for which 14.7 ± 0.2% of the original Ce inventory was released from the wasteform into solution. The extent of Ce leaching into the solution was correlated with the quantity of perovskite present in the wasteform, and associated with the incorporation and preferential dissolution of Ce^{3+}. $CaZr_{0.80}U_{0.20}Ti_{2.00}O_7$ exhibited improved leach resistance relative to $CaZr_{0.80}Ce_{0.20}Ti_{2.00}O_7$, attributed to the decreased proportion of accessory perovskite, with 7.1 ± 0.1% U released to in 8 M HNO_3 after 7 d. The $Ca_{0.80}Zr_{0.90}Ce_{0.30}Ti_{1.60}Al_{0.40}O_7$ composition, with no accessory perovskite phase, presented significantly improved leaching characteristics, with < 0.4%Ce released in both 8 M HNO_3 and 1 M H_2SO_4. These data demonstrate the need for careful compositional design for zirconolite wasteforms with regard to accessory phase formation and surrogate choice.

npj Materials Degradation (2021)5:24; https://doi.org/10.1038/s41529-021-00171-8

INTRODUCTION

Reprocessing of spent Magnox and advanced gas-cooled reactor (AGR) fuels in the UK has resulted in an inventory of PuO_2 forecast to amount to 140 tonnes heavy metal equivalent (teHM). This material is the liability of the Nuclear Decommissioning Authority (NDA), which is supporting the UK government in the Pu management strategy through identifying solutions that put UK civil inventories beyond reach[1]. One approach that satisfies the fundamental criteria of potential disposition pathways is immobilisation within a chemically durable ceramic matrix that incorporates Pu at the atomic scale within a crystalline material, while remaining resistant to the effects of self-irradiation.

Zirconolite, prototypically $CaZrTi_2O_7$, is a naturally occurring titanate mineral that has been identified as a candidate crystalline host phase for Pu immobilisation. The zirconolite-2M polytype (monoclinic unit cell — space group C2/c), where '2M' refers to a two-layer repeated arrangement of cation layers within the unit cell, is stabilised over the solid solution $CaZr_xTi_{3-x}O_7$, with stoichiometry $0.80 \le x \le 1.30$, and is considered the archetype structure[2]. Other zirconolite polytypes are observed as a consequence of the structural rearrangement due to substitution on Ca^{2+}, Zr^{4+}, and Ti^{4+} sites, e.g. 4M, 3T and 3O[3–5]. Substitution of Pu^{4+} on the Zr^{4+} site in zirconolite above 0.15 formula units (f.u.) produces a transformation from a 2 M to 4 M polytype, as reported by Begg et al[6]. Increasing the Pu content in excess of 0.4 f.u. yields the pyrochlore structure, whilst the end member $CaPuTi_2O_7$ is reported to be a fluorite-derivative structure with a reported X-ray amorphisation dose of 1.3×10^{25} α·m^{-3} [7,8]. Zirconolite can also accommodate Pu^{4+} in solid solution through Ca^{2+} site substitution, coupled with co-immobilisation of a suitable charge-balancing species, e.g. $Ca_{1-x}Pu_xZrTi_{2-2x}Al_{2x}O_7$, where Al^{3+} acts as a charge balancing species[9].

The durability of zirconolite for Pu immobilisation (using surrogates for Pu) under conditions relevant for geological disposal is estimated to be of the same order of magnitude as spent nuclear fuel. For example, Meng et al. recently reported the normalised mass loss of Ce in the $Ca_{1-x}Zr_{1-x}Ce_{2x}Ti_2O_7$ system to be of the order 10^{-6}–10^{-7} g m^{-2} when leached in H_2O at 90 °C[10]. The normalised release rate of Nd from single-phase Nd-doped zirconolite-2M was reported to be 10^{-5} g m^{-2} d^{-1} by Cai et al. over a 42-d period[11]. Since the dissolution rate is inherently low, accelerated leaching methods can be utilised to rapidly evaluate the dissolution of zirconolite ceramics of different compositions and structures. Such acceleration could be promoted by increasing the reactive surface area exposed to the solution, by increasing the temperature, or by using aggressive leaching media, such as strong acid or alkali solutions. For example, Strachan et al.[12] and Icenhower et al.[13] undertook the assessment of the forward rate of dissolution of Pu and Ce in zirconolite and less-durable pyrochlore materials, respectively, at pH 2, since this was the only solution condition under which elements were measurable. The latter approach is also of relevance to understand the recovery of fissile inventory from such a material, should there be a future need to rework the wasteform or reverse the decision to immobilise in favour of reuse.

While the durability of zirconolite is relatively high, should processing conditions result in the formation of accessory phases that readily partition Pu, the rate of Pu release during dissolution may be enhanced. $CaTiO_3$ perovskite is one such accessory phase that is postulated to increase the release of Pu to aqueous leaching media, largely informed by early durability trials of the SYNROC-C wasteform, for which zirconolite and perovskite were included as hosts for actinides[14]. The extent of perovskite formation can also be dependent on the choice surrogate used

[1]Immobilisation Science Laboratory, University of Sheffield, Department of Materials Science and Engineering, Sheffield, UK. [2]National Nuclear Laboratory, Workington, Cumbria, UK. ✉email: c.corkhill@sheffield.ac.uk

for Pu, typically Ce or U, and the prevailing oxygen fugacity during synthesis[3,15].

In this study, we aim to quantify the release of Pu surrogates from zirconolite to a range of aggressive leaching media, to provide a greater understanding of the effect of (i) media composition; (ii) contribution of perovskite accessory phase; and (iii) Pu surrogate choice (Ce or U) on the durability of zirconolite ceramics. To achieve this, three different zirconolite compositions were investigated. Firstly, a 'non-ideal' formulation of $CaZr_{0.80}M_{0.20}Ti_{2.00}O_7$, with a minor perovskite accessory phase, was investigated, with $M = Ce^{4+}$ or $M = U^{4+}$ as surrogates for Pu^{4+}. The third composition targeted $Ca_{0.80}Zr_{0.90}Ce_{0.30}Ti_{1.60}Al_{0.40}O_7$, reformulated with approximately 0.10 f.u. excess each of both Ti and Zr, added to preclude the formation of perovskite and accommodate partial Ce^{3+} speciation, resulting in a nominal composition of $Ca_{0.80}Zr_{1.00}Ce_{0.30}Ti_{1.70}Al_{0.40}O_7$. The characterisation of these phases is first described, followed by an evaluation of their leaching behavior.

RESULTS AND DISCUSSION

Phase assemblage and redox chemistry

Monoclinic zirconolite-2M (space group C2/c) was identified as the major crystalline phase (~80 wt.%) for the $CaZr_{0.80}Ce_{0.20}Ti_{2.00}O_7$ formulation (Fig. 1a and Table 1). The unit cell parameters were determined by Rietveld analysis of the powder diffraction profile to be $a = 12.4898(2)$ Å, $b = 7.2807(1)$ Å, $c = 11.3979(2)$ Å, $\beta = 100.593(1)^\circ$ and $V = 1018.81(2)$ Å^3. Inspection of the powder diffraction profile revealed reflections attributed to other, minor, phases. The first of these was zirconolite-4M (~10 wt.%), which was distinguished via the presence of diagnostic supercell reflections (002) and (008) at $2\theta = 7.8^\circ$ and $2\theta = 31.1^\circ$, respectively. This phase was also apparent in SEM images, clearly distinguished by the contrast variation in the back-scattered electron image and by a cerium enrichment, as shown in the Ce-Lα EDS data (Supplementary Fig. 1).

Ce-bearing perovskite (nominal composition $(Ca,Ce)TiO_3$) was also identified. This phase, preferentially accommodating Ce in reduced form (Ce^{3+}), has previously been observed to form during HIP synthesis of zirconolite, as a result of the reducing environment imposed by the in-canister containment[16]. The presence of Ce^{3+} was confirmed by X-ray absorption near-edge structure (XANES) spectroscopy; linear combination analysis revealed that 59 ± 3 at.% of the Ce inventory was reduced to the Ce^{3+} species (Supplementary Fig. 2). A small amount of unreacted ZrO_2 (<1 wt.%) and trace CeO_2 (identified by SEM/EDS only), considered to be artefacts of the milling process, were also observed.

The phase assemblage obtained for the U-bearing zirconolite counterpart, $CaZr_{0.80}U_{0.20}Ti_{2.00}O_7$, comprised primarily zirconolite-2M (~97 wt.%—Table 1) with unit cell dimensions $a = 12.4779(27)$ Å, $b = 7.2424(21)$ Å, $c = 11.3899(30)$ Å, $\beta = 100.651(33)^\circ$ and $V = 1011.58(27)$ Å^3 (Fig. 1b). A number of other XRD reflections were distinguished, corresponding to trace phases of perovskite and UO_2. Two distinct ZrO_2 phases were also observed by SEM, consistent with ZrO_2, and a $(Zr,U)O_2$ dilute solid solution (Supplementary Fig. 3). Given the pseudo-binary phase diagram of PuO_2-ZrO_2, it is plausible that Pu counterpart formulations may contain a $(Zr,Pu)O_2$ solid solution[17,18]. However, to our knowledge, no such phases have previously been reported in the literature pertaining to Pu-zirconolite, even at relatively high Pu loadings[4].

It is possible that a portion of the available U may have been accommodated within the accessory perovskite phase, with U stabilised as U^{4+}. In such a case, charge balance is provided by partial reduction of Ti^{4+} to Ti^{3+} in the $CaTiO_3$ structure, as was reported by Vance et al[19]. However, it was not possible to reliably distinguish perovskite grains from the bulk zirconolite-2M phase by SEM (Supplementary Fig. 3) due to a combination of fine grain structure, low occupation within the microstructure (<1 wt.%), and similar backscattered electron coefficient. Therefore, the incorporation, and extent thereof, of U in the perovskite phase could not be definitively confirmed.

Uranium L_3 XANES spectra were obtained to determine whether the redox environment in the canister was sufficient to maintain

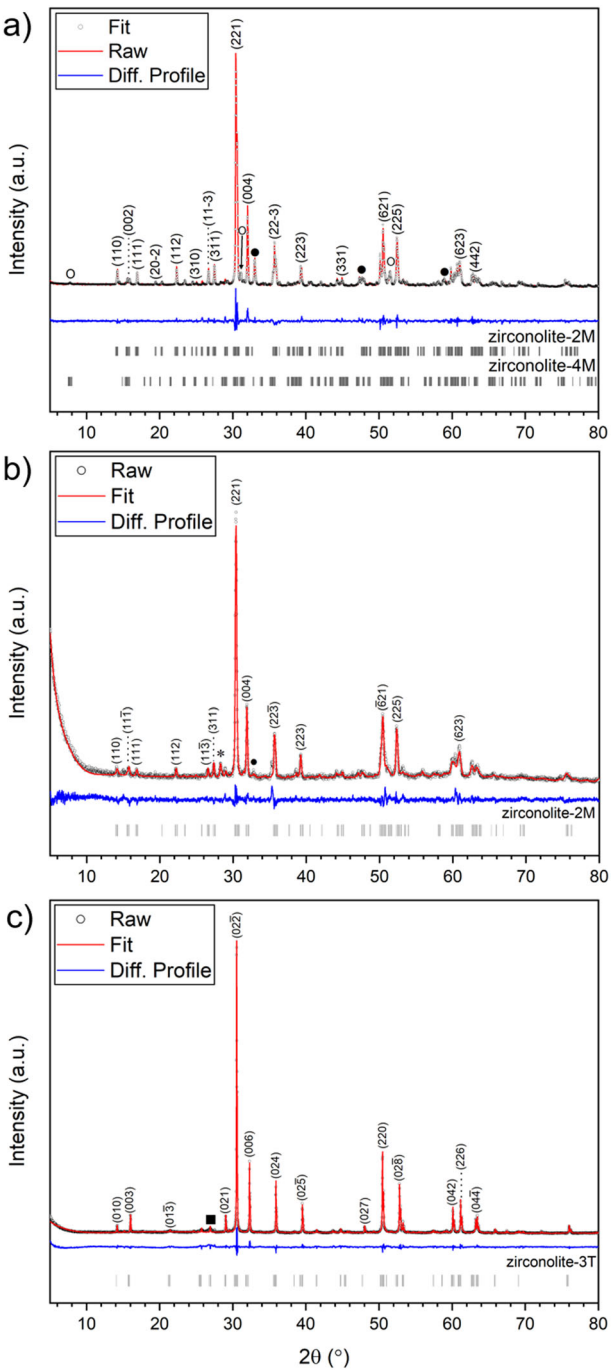

Fig. 1 Refined powder diffraction profiles of zirconolite ceramic materials. Showing **a** HIPed $CaZr_{0.80}Ce_{0.20}Ti_{2.00}O_7$; **b** HIPed $CaZr_{0.80}U_{0.20}Ti_{2.00}O_7$; and **c** CPS $Ca_{0.80}Zr_{0.90}Ce_{0.30}Ti_{1.60}Al_{0.40}O_7$. Zirconolite-2M, 4 M, and 3T reflections are indexed with corresponding (hkl) values. Diagnostic zirconolite-4M reflections are labelled with open circles (o). Perovskite reflections are labelled with closed circles. UO_2 reflections are labelled with asterisks. Al_2TiO_5 reflections are labelled with closed squares.

Table 1. Phase assemblage of zirconolite materials, as determined by Rietveld analysis of powder XRD data shown in Fig. 1.

Phase	$CaZr_{0.80}Ce_{0.20}Ti_{2.00}O_7$	$CaZr_{0.80}U_{0.20}Ti_{2.00}O_7$	$Ca_{0.80}Zr_{0.90}Ce_{0.30}Ti_{1.60}Al_{0.40}O_7$
Zirconolite-2M	81.06 ± 0.04	97.08 ± 0.02	–
Zirconolite-4M	9.6 ± 0.1	–	–
Zirconolite-3T	–	–	98.4 ± 0.6
Perovskite	8.7 ± 0.1	0.94 ± 0.61	–
ZrO_2	0.67 ± 0.04	–	–
UO_2	–	0.62 ± 0.12	–
$Zr_{1-x}U_xO_2$	–	1.34 ± 0.60	–
Al_2TiO_5	–	–	1.6 ± 0.6

The reported precision of phase fractions represents the uncertainty associated with parameter fitting in the Rietveld analysis.

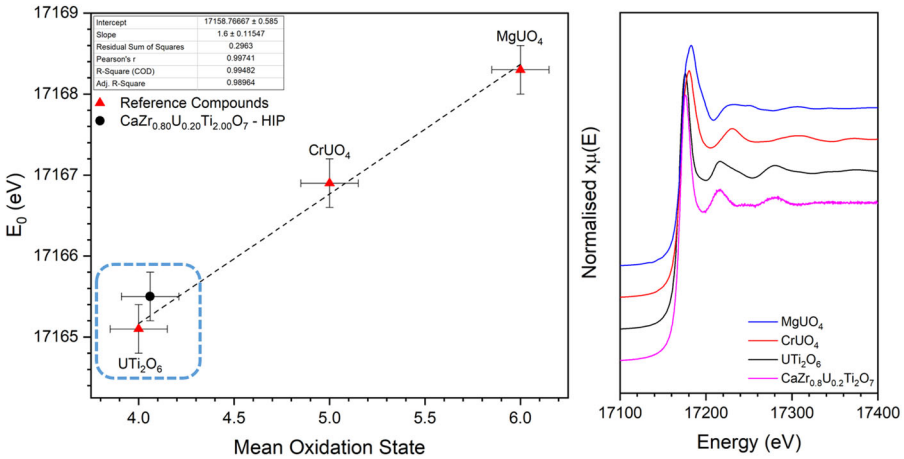

Fig. 2 U L_3 XANES data for $CaZr_{0.80}U_{0.20}Ti_{2.00}O_7$ alongside $U^{4+}Ti_2O_6$, $CrU^{5+}O_4$ and $MgU^{6+}O4$ reference compounds. Error bars represent the error on the linear regression of edge position of the samples to the edge position of known standards.

the target U^{4+} oxidation state (Fig. 2). Two key features of the data qualitatively indicated a U^{4+} valence: the white line features of the $CaZr_{0.80}U_{0.20}Ti_{2.00}O_7$ U L_3 absorption edge were similar to that of the $U^{4+}Ti_2O_6$ reference compound, while the edge positions of the $CrU^{5+}O_4$ and $MgU^{6+}O_4$ reference compounds were clearly shifted to higher energy when compared to $CaZr_{0.80}U_{0.20}Ti_{2.00}O_7$. The mean oxidation state of U in $CaZr_{0.80}U_{0.20}Ti_{2.00}O_7$ was determined by linear regression of the E_0 position, with respect to standards of known oxidation state, to be 4.06 ± 0.30. This confirms that the HIP environment was sufficiently reducing to maintain U as U^{4+}.

Inspection of the powder XRD data obtained for the reformulated $Ca_{0.80}Zr_{0.90}Ce_{0.30}Ti_{1.60}Al_{0.40}O_7$ composition (Fig. 1c) was consistent with the formation of single-phase zirconolite-3T, occupying the space group $P3_121$. It is important to note that this composition did not yield perovskite as a secondary phase, meaning the entire Ce inventory was contained wholly within the zirconolite-3T phase. This is attributed to the fact that the reformulated $Ca_{0.80}Zr_{0.90}Ce_{0.30}Ti_{1.60}Al_{0.40}O_7$ composition incorporated excess Zr and Ti as buffer phases and was synthesised by sintering under an air atmosphere, rather than by HIP. A satisfactory Le Bail fit was obtained using the structural model reported by Grey et al. for which single-crystal X-ray diffraction data of the synthetic $Ca_{0.80}Zr_{1.30}Th_{0.15}Ti_{1.35}Al_{0.40}O_7$ phase was published[20]. Although there are limited detailed structural analyses of the synthetic zirconolite-3T phase reported in the wider literature, the refinement statistics were satisfactory (R_p = 7.96%, R_{wp} = 10.29%). The output from this refinement produced cell parameters for the zirconolite-3T phase calculated to be a = 7.2377(2) Å, c = 16.6621(4) Å, and V = 755.90(4) Å^3. Close inspection of powder XRD data revealed minor reflections consistent with a pseudobrookite structured phase (nominally Al_2TiO_5), accounting for approximately 1.6 wt.% of the phase assemblage, presumably formed as a reaction product due to the excess 0.1 f.u. TiO_2. SEM-EDS analyses (Supplementary Fig. 4) confirmed the presence of an Al and Ti-containing phase present as an accessory phase within the zirconolite-3T matrix. EDS analysis established that the surrogate Ce fraction was not incorporated within this phase. The average composition of the zirconolite phase was calculated to be $Ca_{0.78(3)}Zr_{0.80(3)}Ce_{0.23(2)}Ti_{1.81(2)}Al_{0.39(2)}O_7$, normalised to seven oxygen atoms.

Perovskite influence on HIPed Ce-zirconolite leaching

Two successive static leaching experiments were performed on powdered material for each zirconolite composition, in a range of aggressive media at 90 °C, over a period of 7 d each (Fig. 3). Leaching data are reported and discussed, with reference to specific elements, as a function of the leaching efficiency from the ceramic wasteform material into the leaching solution. In this instance, a leaching efficiency of 100% Ce would represent the complete dissolution of the surrogate fissile inventory from the wasteform into solution. For $CaZr_{0.80}Ce_{0.20}Ti_{2.00}O_7$, in the first stage of leaching, the greatest level of Ce dissolution was achieved in 1M H_2SO_4; the elemental release of Ce in this medium was 14.7 ± 0.2% (Fig. 3a, Supplementary Table 1). Ca was preferentially dissolved into the leachate with respect to Ti, and Zr dissolution was considerably lower. The extent of elemental release in the first leaching step, under all leaching conditions, followed the same trend (Ce > Ca > Ti >> Zr), with the exception of 1M NaOH, which

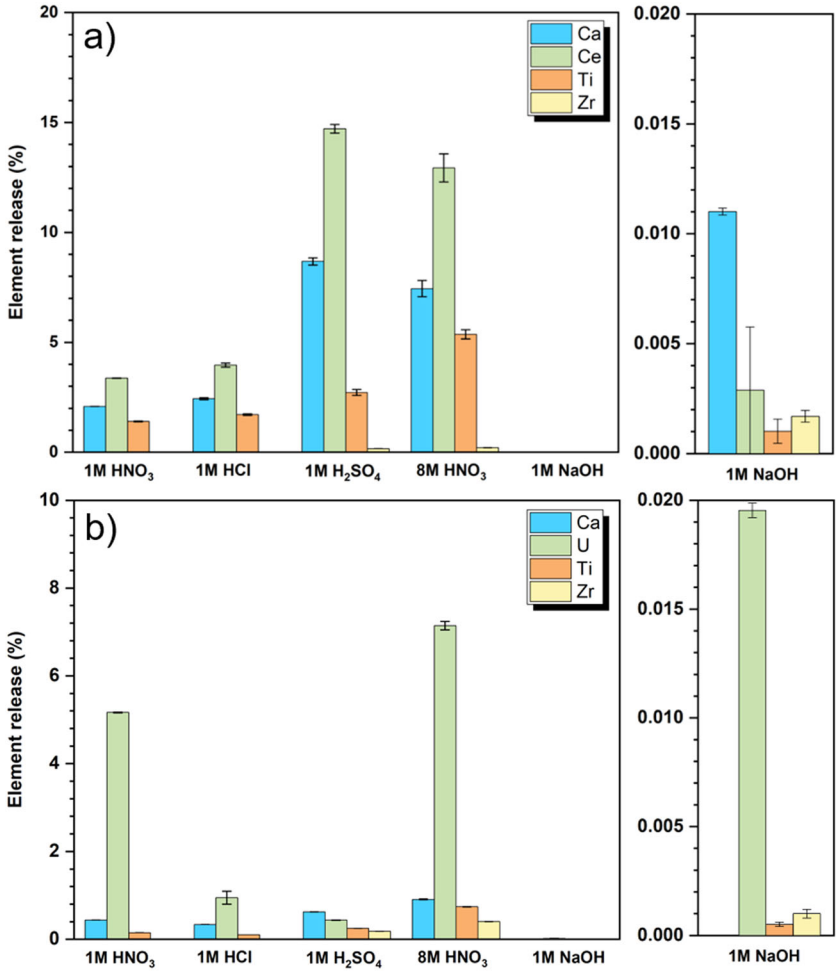

Fig. 3 Elemental release (%) of Ca, Ce, U, Zr and Ti from zirconolite samples into the aqueous leaching media. Showing results for **a** $CaZr_{0.80}Ce_{0.20}Ti_{2.00}O_7$ **b** $CaZr_{0.80}U_{0.20}Ti_{2.00}O_7$. Error bars represent the standard deviation of duplicate measurements.

exhibited extremely low elemental release. When exposed to 8M HNO_3, 12.9 ± 0.7% of the Ce inventory was dissolved into the leachate, indicating that the use of 8M HNO_3 or 1M H_2SO_4 resulted in the greatest extraction of the Ce surrogate. Similar behaviour was observed in the leaching of ThO_2, where sulphuric acid was more efficient at leaching Th than nitric and hydrochloric acid[21]. This was attributed to the higher strength of the metal–ligand complex for sulfate than for chloride or nitrate. The extent of elemental release was lower in the presence of 1M HNO_3 and 1M HCl, with the Ce release measured as 3.37 ± 0.01% and 4.0 ± 0.1%, respectively. A similar elemental release was observed for the other elements in these media and, in both cases, the leaching of Zr was negligible. The wasteform was most resistant to elemental extraction in the presence of 1M NaOH, with Ce extraction measured as 0.003 ± 0.003%.

After the termination of the first leaching experiment, the ceramic powders were recovered, washed with isopropanol, and the surface was examined by SEM, as shown in Fig. 4. The degree of visible surface damage, relative to the pristine material (Supplementary Fig. 5), was consistent with the extent of dissolution for each medium; for example, the specimens exposed to 1M H_2SO_4 and 8M HNO_3 presented the most visible surface degradation, in agreement with the higher percentage of elements released to these solutions. The presence of pitting may be an artefact of surface morphology or incongruent dissolution associated with the presence of multiple phases. No visible damage was observed for material recovered from 1M NaOH solution (data not shown).

High-magnification observations of specimens leached in 8M HNO_3 and 1M H_2SO_4 exposed the presence of small surface precipitates, approximately 1 μm in diameter (Figs. 4 and 5). EDS analysis revealed that they were enriched in Ti and O, and geochemical modelling indicated that TiO_2 (anatase and rutile) was saturated in solution; both suggest the precipitation of Ti from the leachate onto the ceramic surface. TiO_2 precipitation has previously been reported during perovskite dissolution[22,23], indicating that Ti may have been preferentially dissolved from the ceramic wasteform via the mechanism outlined by Pham et al.[24] in Eq. 1. It is inferred that the decomposition of $Ti(OH)_x^{(4-x)+}$ under hydrothermal conditions (i.e. T ≥ 90 °C) drives the nucleation and growth of TiO_2. The spherical morphology of these precipitates is consistent with those presented in similar work[25].

$$CaTiO_3 + (6-x)H^+_{(aq)} \rightarrow Ca^{2+}_{(aq)} + Ti(OH)_x^{(4-x)+} + (3-x)H_2O \quad (1)$$

To confirm whether the perovskite phase was preferentially leached, powder XRD data were collected on recovered specimens, to ascertain the amount of perovskite present after leaching relative to the pristine composition (Fig. 6). The relative intensity of the dominant perovskite reflection ($2\theta = 33.1^\circ$) was observed to decrease after leaching in all media, confirming that this phase was preferentially leached from the wasteform. In agreement with the elemental release results presented in Fig. 3, the 1M H_2SO_4 medium was most effective at leaching perovskite, with 2.6 ± 0.2

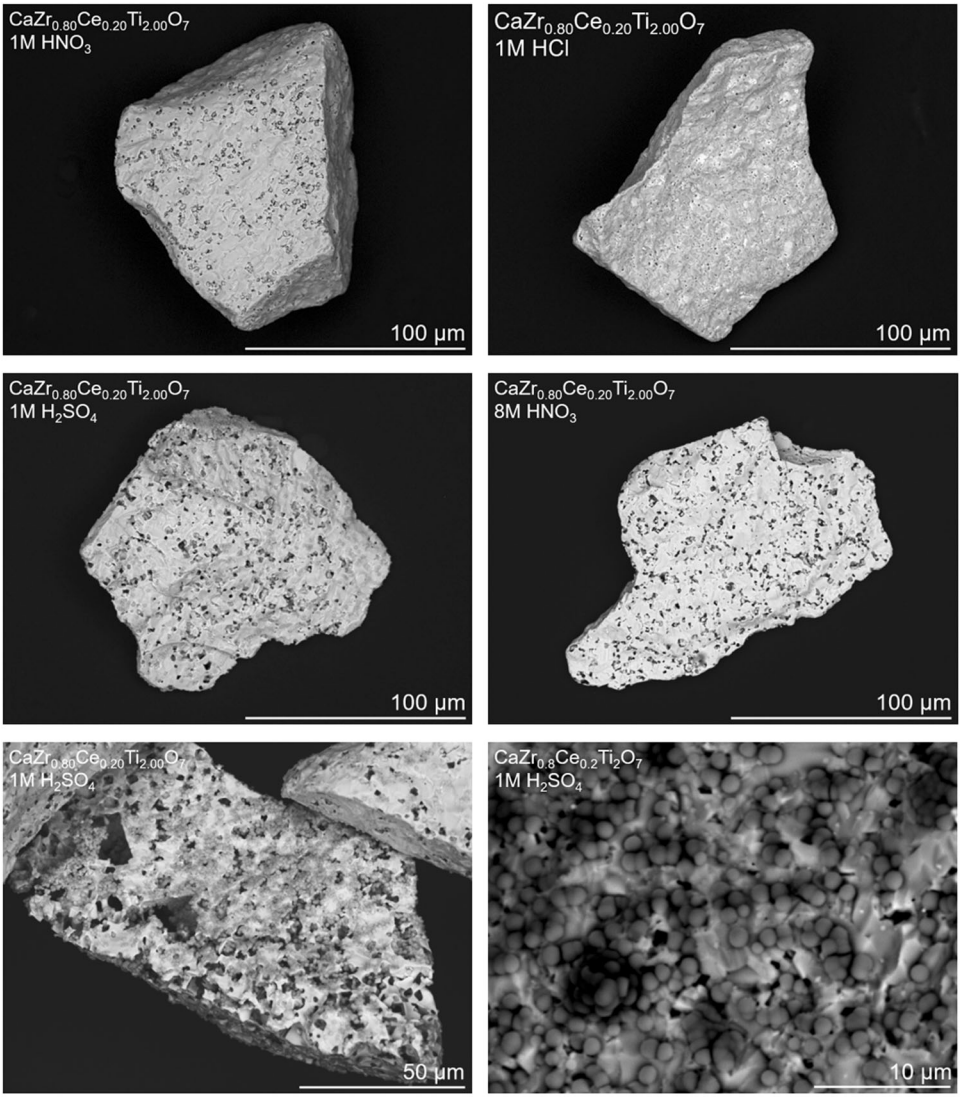

Fig. 4 SEM examination of $CaZr_{0.80}Ce_{0.20}Ti_{2.00}O_7$ ceramics exposed to 1M HCl, 1M HNO_3, 1M H_2SO_4, and 8M HNO_3 at 90 °C for 7 d. The scale bar on the upper 4 images is 100 µm, the bottom left is 50 µm and the bottom right, 10 µm.

wt.% remaining (corresponding to around two-thirds of the original perovskite fraction dissolved), as determined by Rietveld analysis of powder diffraction data collected on samples of the recovered material. Following dissolution in 8M HNO_3, an aqueous environment similar to that imposed during aqueous reprocessing of spent nuclear fuel, around one-third of the original perovskite fraction remained. It is important to note that the zirconolite-2M or zirconolite-4M reflections did not decrease relative to one another, indicating these phases may exhibit similar durability. Nevertheless, we acknowledge that the quantification of the phases based on powder XRD data is an artefact of the refinement output, and may not be entirely physically representative of the system.

XANES data were acquired at the Ce L_3 edge for specimens recovered after leaching (Table 2 and Supplementary Fig. 2). Comparison of the pristine and leached samples showed that the oxidation state of Ce in all cases was a combination of Ce^{3+} and Ce^{4+} however, subtle differences in the intensity of the doublet features for the leached samples were observed. Linear combination fitting (Table 2) revealed a small decrease in the Ce^{3+} content, from 59 ± 3 at.% Ce^{3+} in the pristine sample to 49 ± 3 at.% Ce^{3+} for zirconolite leached in 1M H_2SO_4 and 48 ± 3 at.% Ce^{3+} for 8M HNO_3. These values are consistent with preferential perovskite leaching. The relatively high fraction of Ce^{3+} present in the pristine sample was attributed to the reducing conditions imposed by the Cr/Fe-rich stainless steel containment using for HIP processing. While Ce^{3+} is preferentially accommodated in the Ca^{2+} site in perovskite, some of the Ce^{3+} inventory must also be located within the zirconolite phase. This is unsurprising, as we have previously demonstrated that considerable Ce^{3+} content may be present in single-phase zirconolite-2M[26]. Furthermore, Meng et al. confirmed that approximately 51% Ce^{3+} could be accommodated across a mixture of zirconolite-2M and -4M polytypes, in broad agreement with the Ce speciation presented here[10].

A second leaching experiment in fresh media was performed on the specimens that contained less than 4 wt.% perovskite after the first leaching (i.e. material leached in 1M H_2SO_4 and 8M HNO_3). The aim was to quantify the extent of Ce released after most of the accessible perovskite had been removed. After a further 7 d at 90 °C, the concentrations of Ca, Ce and Ti dissolved in the leachate were significantly reduced (Fig. 7 and Supplementary Table 2), from ~13% Ce in the first leaching step to 2.03 ± 0.01% and 3.46 ± 0.02% Ce release for 1M H_2SO_4 and 8M HNO_3, respectively, as a percentage of the remaining Ce inventory subsequent to the primary leaching trial. Therefore, it is evident that the accessory perovskite phase was the major contributor to Ce release in the first leaching step.

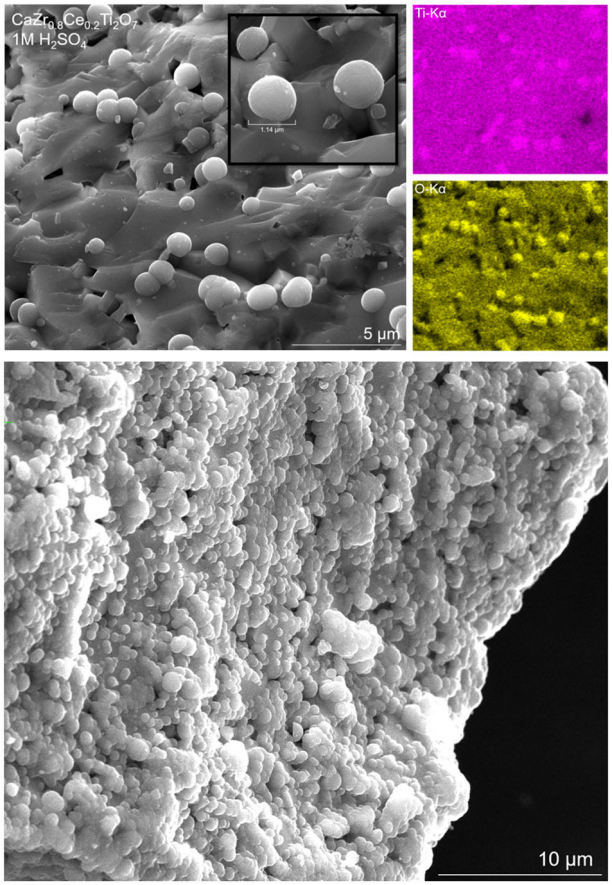

Fig. 5 SEM-EDS analysis of titanium-rich surface precipitates observed on $CaZr_{0.80}Ce_{0.20}Ti_{2.00}O_7$ particulates recovered from 1 M H_2SO_4 solution at 90 °C for 14 days (cumulative leaching time). The upper SEM image has a scale bar of 5 µm and the spherical precipitate is ~1 µm in size. The EDS images are Ti (pink) and O (yellow). The lower image has a scale bar of 10 µm.

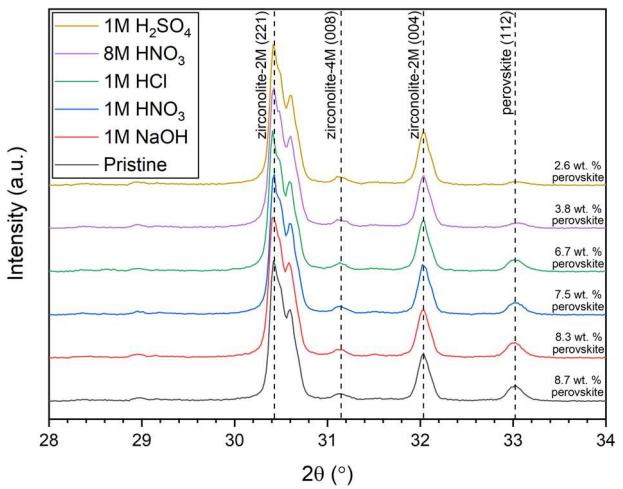

Fig. 6 Powder XRD data for $CaZr_{0.80}Ce_{0.20}Ti_{2.00}O_7$ following leaching at 90 °C for 7 days. The remaining amount of perovskite, relative to the pristine sample, was determined by Rietveld analysis of powder diffraction data for recovered material.

It should be noted that, despite thorough washing between leaching steps, spherical precipitates of TiO_2 were observed on the surface of specimens leached in 1M H_2SO_4 after the second leaching step in fresh media (Fig. 5). Geochemical modelling indicated that gypsum ($CaSO_4$) was saturated in solution for the H_2SO_4 medium in both leaching steps. Although there was no evidence for the formation of this phase, which is unlikely to precipitate in the strongly acidic medium, the modelling results suggest that calcium sulfate complexes are thermodynamically favourable under the conditions of the experiment. This may indicate the preferential leaching of Ca-containing phases and, when combined with the observation of TiO_2 precipitates, we hypothesise that even very low amounts of perovskite (~2 wt.%) can be dissolved, resulting in the formation of secondary phases. The Ce release within the 1M H_2SO_4 medium was somewhat lower than that in HNO_3 (Fig. 7), despite the fact that after leaching in HNO_3 the recovered product contained slightly more perovskite (3.8 wt.% and 2.6 wt.% for 8M HNO_3 and 1M H_2SO_4, respectively). Therefore, it is possible that the TiO_2 surface layer passivated the dissolution reaction to a certain extent, protecting the underlying ceramic from further corrosion. Further studies are required to investigate the passivating nature of this layer.

Table 2. Ce speciation (at.%) in $CaZr_{0.80}Ce_{0.20}Ti_{2.00}O_7$ determined by linear combination fitting of Ce L_3 XANES data with respect to Ce^{3+} and Ce^{4+} reference compounds.

Specimen	Ce speciation (at. %)		*R*-factor
	Ce^{3+}	Ce^{4+}	
$CaZr_{0.80}Ce_{0.20}Ti_{2.00}O_7$ — Pristine	59 ± 3	41 ± 3	0.0419
$CaZr_{0.80}Ce_{0.20}Ti_{2.00}O_7$ — 8 M HNO_3	48 ± 3	52 ± 3	0.0408
$CaZr_{0.80}Ce_{0.20}Ti_{2.00}O_7$ —1 M HNO_3	49 ± 3	51 ± 3	0.0503

Reported errors represent the error on the linear combination fit with reference to known standard data.

Plutonium surrogate leaching

To evaluate the influence of fissile surrogate choice on the leaching behavior, $CaZr_{0.80}U_{0.20}Ti_{2.00}O_7$ was subjected to the same accelerated leaching as $CaZr_{0.80}Ce_{0.20}Ti_{2.00}O_7$. Data for the first leaching step are shown in Fig. 3b and Supplementary Table 1, and the second step in Fig. 7 and Supplementary Table 2. In contrast to the first leaching of $CaZr_{0.80}Ce_{0.20}Ti_{2.00}O_7$ (Fig. 3a), the greatest release of U into the leaching medium was stimulated by 8M HNO_3, corresponding to a release of 7.1 ± 0.10%. Release fractions of the other constituents Ca, Ti and Zr were considerably lower than for U (Supplementary Table 1). As observed for the Ce-counterpart zirconolite, the element release generally followed the trend of surrogate (U) > Ca > Ti >> Zr under all conditions, with the exception of 1M H_2SO_4, in which a marginally greater amount of Ca was detected in the aqueous phase than U. As detailed previously, this is indicative of the preferential leaching of Ca from the minor accessory perovskite. The second highest degree of leaching was observed for 1M HNO_3 medium, resulting in 5.17 ± 0.01% U release. The zirconolite formulated with U was clearly more susceptible to leaching in HNO_3 media, whereas the Ce counterpart composition was preferentially leached in H_2SO_4. This is due to the oxidation of U^{4+} within the zirconolite structure (Fig. 2) to the highly soluble uranyl (U^{6+}) nitrate complex, a mechanism that is not available in the case of Ce^{4+} since it is already in its most oxidised form. While geochemical modelling indicated that polymorphs of TiO_2 were saturated in solution, SEM analysis of $CaZr_{0.80}U_{0.20}Ti_{2.00}O_7$ material recovered from solution did not evidence spherical TiO_2 precipitates. The lack of TiO_2 was attributed to the lower occupation of perovskite in the microstructure when compared with $CaZr_{0.80}Ce_{0.20}Ti_{2.00}O_7$.

Leaching in 1M HCl and 1M H_2SO_4 was less aggressive when compared to the HNO_3 solutions, with 0.9 ± 0.2% and ~0.4% of the

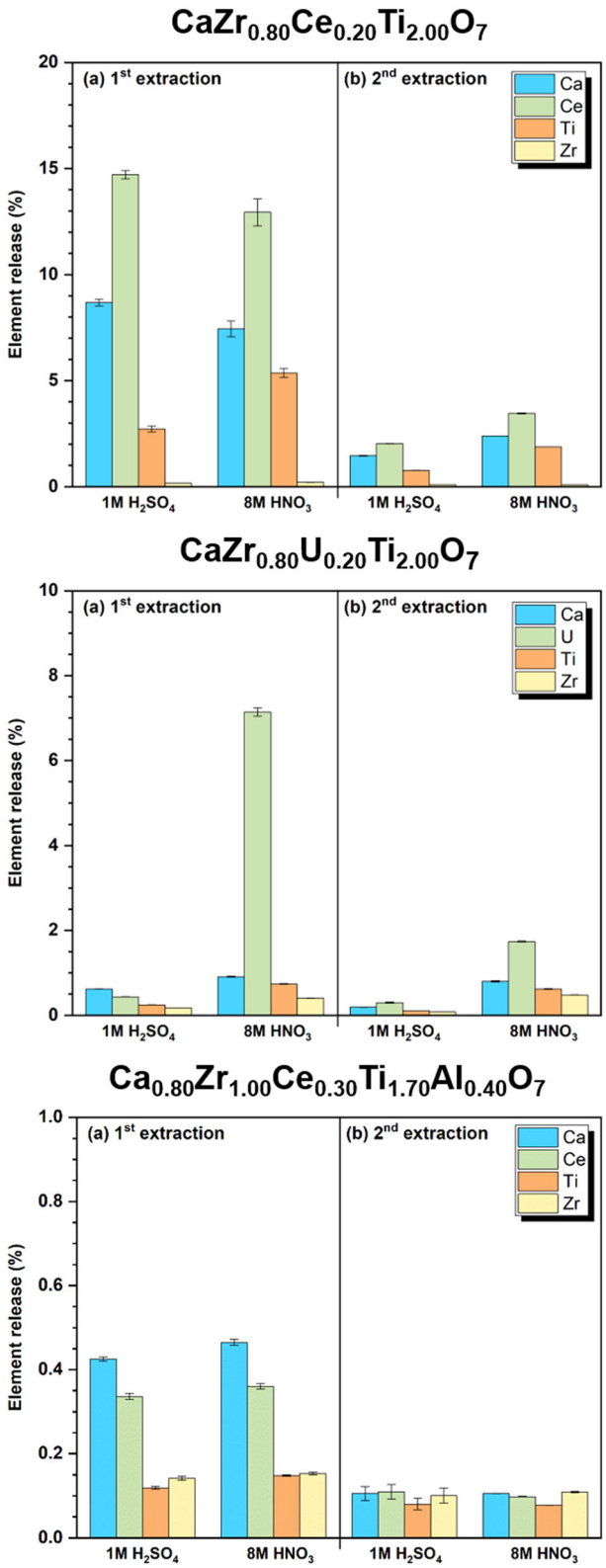

Fig. 7 Elemental release (%) for Ca, Ce, U, Ti and Zr measured for first and second leaching of $CaZr_{0.80}Ce_{0.20}Ti_{2.00}O_7$, $CaZr_{0.80}U_{0.20}Ti_{2.00}O_7$ and reformulated $Ca_{0.80}Zr_{0.90}Ce_{0.30}Ti_{1.60}Al_{0.40}O_7$ in 1M H_2SO_4 and 8M HNO_3, determined by ICP-OES analysis. Error bars represent the standard deviation of duplicate measurements.

initial U inventory dissolved from the ceramic, respectively. As with the corresponding Ce composition, a negligible release fraction was measured for each constituent element when exposed to 1M NaOH solution, as shown in the inset to Fig. 3 (b). Despite this, the concentration of U detected in the leachate amounted to a loss of 0.02 % U, with the remaining elements <0.001%.

In accordance with the procedure applied for the $CaZr_{0.80}Ce_{0.20}Ti_{2.00}O_7$ composition, the U-counterpart zirconolite specimens exposed to 8M HNO_3 and 1M H_2SO_4 were recovered and washed, prior to a second leaching step under identical conditions (Fig. 7). The amount of U released was significantly lower than in the first leaching step; in 8M HNO_3, only $1.7 \pm 0.01\%$ U was released into solution after the second leaching, compared to ~7% in the first. This decrease indicates that the first leaching step effectively removed accessory U-containing phases, which constituted less than 2 wt.% of the pristine phase assemblage (Table 1). The ceramic material remained largely resistant to leaching in 1M H_2SO_4 in the second leaching step, with only $0.30 \pm 0.01\%$ of the remaining U released into solution.

Given the fact that the Ce-containing counterpart still contained perovskite after the first leaching, which was particularly susceptible to leaching in 1M H_2SO_4, it is difficult to make a direct comparison between the leach rates of the two Pu surrogates, Ce and U, contained with the primary zirconolite phase. However, these results indicate that accessory phases in zirconolite materials, formulated using both surrogates, can strongly influence the dissolution of the Pu surrogate. Since $CaZr_{0.80}U_{0.20}Ti_{2.00}O_7$ contained less perovskite, the overall leach rates were lower, however, accessory U-containing phases were susceptible to oxidative leaching in HNO_3.

Accelerated leaching of reformulated Ce-zirconolite

Since the extent of dissolution in all media except 1 M H_2SO_4 and 8 M HNO_3 was negligible, the $Ca_{0.80}Zr_{0.90}Ce_{0.30}Ti_{1.60}Al_{0.40}O_7$ material was subjected to leaching in these media only. As previously noted this reformulated composition did not contain perovskite as an accessory phase. Results of the first leaching are shown in Fig. 7 and Supplementary Table 1; the Ce release was similar in both solutions, at $0.36 \pm 0.01\%$ and $0.34 \pm 0.01\%$ Ce, respectively. Recovery of material, washing, and subsequent introduction to fresh solution resulted in the lowest elemental release for all samples in the study (Supplementary Table 2). The Ce release was the same, within error, at $0.11 \pm 0.02\%$ and $0.098 \pm 0.001\%$, for 1M H_2SO_4 and 8M HNO_3, respectively. Clearly, the concentration of each element released from the $Ca_{0.80}Zr_{0.90}Ce_{0.30}Ti_{1.60}Al_{0.40}O_7$ ceramic formulation was significantly lower (on the order of tenfold in most instances) than the previous formulations containing accessory phases. Interestingly, the general trend in elemental release that was observed previously (Ce > Ca > Ti > Zr) was not observed after either leaching step; rather, each element was released congruently. These data confirm the high aqueous durability of single-phase zirconolite, even in extremely aggressive media. Geochemical modelling confirmed that TiO_2 polymorphs were saturated in solution for both 1M H_2SO_4 and 8M HNO_3 leaching media; nonetheless, SEM analysis of the recovered material failed to evidence surface precipitates.

Compositional design and surrogate choice

There was a marked improvement in the acid leaching resistance of all materials when accessory phases were eliminated. Accordingly, in the case of the reformulated $Ca_{0.80}Zr_{0.90}Ce_{0.30}Ti_{1.60}Al_{0.40}O_7$

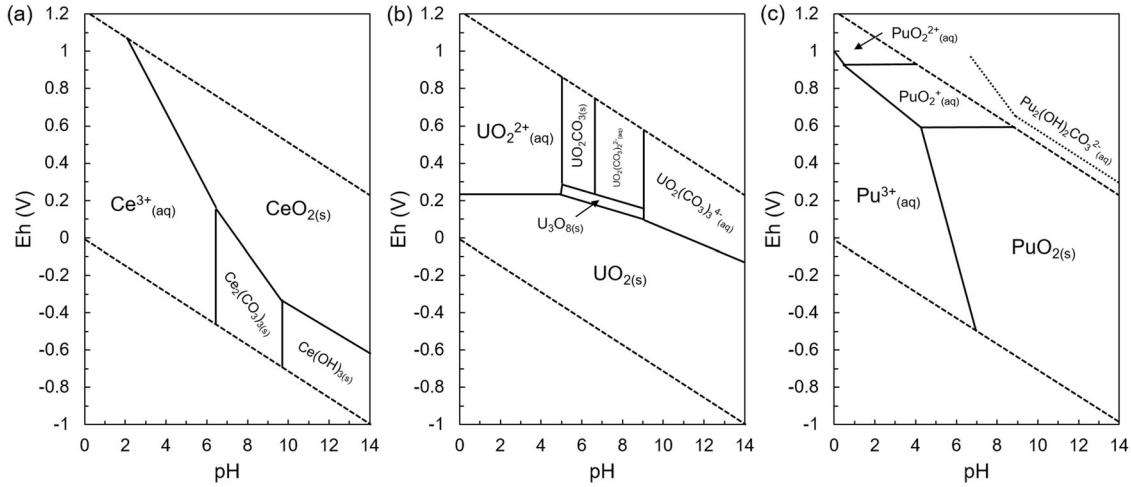

Fig. 8 Pourbaix diagrams for Ce, U and Pu. Showing **a** the Ce–C–O–H system; **b** the U–C–O–H system; and **c** the Pu–(C)–O–H system all at 25 °C and 1 bar, with 10^{-6} M Ce, U and Pu, and 10^{-3} M C. C is included since the experiments were performed in equilibrium with atmosphere CO_2. Adapted from Brookins[33].

composition, which was designed to preclude accessory phases, the resistance to leaching was extremely high. The presence of perovskite was particularly detrimental to leach resistance, with the effects most strongly evident in the Ce-containing $CaZr_{0.80}Ce_{0.20}Ti_{2.00}O_7$ composition.

Ce^{3+}-bearing perovskite formation during zirconolite synthesis is well documented. Clark et al. reported the stabilization of $Ca_{0.4}Ce_{0.4}TiO_3$ perovskite during the synthesis of zirconolite with stoichiometry $CaZr_{1-x}Ce_xTi_2O_7$ under reducing conditions[26]. Similarly, Blackburn et al. stabilised a Ce-bearing perovskite phase during synthesis of zirconolite using highly reducing spark plasma sintering[27]. The partial reduction of the Ce inventory to Ce^{3+} (1.34 Å in 12-fold coordination) presumably stabilises the perovskite phase due to greater compatibility with the 12-fold coordinated Ca^{2+} site (1.34 Å), with respect to the eightfold coordinated Ca^{2+} site in the zirconolite structure (1.12 Å). Since Ce^{3+} is more soluble than Ce^{4+}, especially under the acidic conditions of the experiments performed in the present study (Fig. 8), it is this Ce^{3+}-containing perovskite that preferentially dissolves in aqueous media.

This behaviour did not occur to the same extent in $CaZr_{0.80}U_{0.20}Ti_{2.00}O_7$, although the lower elemental release of all elements from this material during the second leaching step indicates that accessory U-containing phases may be less stable than zirconolite. These phases were identified as UO_2, $(Zr,U)O_2$ and perovskite, although it was not possible to confirm that perovskite contained U.

Since the reformulated composition contained no perovskite, there was no capacity for segregation of soluble Ce^{3+} from the main zirconolite-3T phase. The suppression of the accessory perovskite phase, into which Ce^{3+} preferentially partitions, was achieved through compositional reformulation whereby an excess of Zr and Ti were present. The application of such a wasteform design philosophy, in which ideal compositions are reformulated to account for potential variations in valence state, i.e. partial Ce^{3+} speciation, has clear implications for the fabrication of Pu-bearing ceramic phases related to the zirconolite system. Nevertheless, it is understood that the susceptibility of Pu^{4+} to reduce to the Pu^{3+} species, under the given conditions, is notably lower than for Ce^{3+} [9]. Hence, the capacity for Pu^{3+} segregation into a secondary perovskite phase, and thus premature release under acidic leaching conditions, is markedly reduced with respect to Ce^{3+}.

Comparison of the Pourbaix diagrams for Ce and U (Fig. 8a and b) shows that in aqueous media, these elements are expected to behave differently, largely on account of the propensity for oxidation of U^{4+} to aqueous U^{6+} species. According to these diagrams, provided Ce remains in its tetravalent state, it should be stable across a wide range of redox conditions. This explains the low level of Ce release exhibited in 1M NaOH, with pH 12. In accordance with Fig. 8a, if any Ce^{3+} is present within accessory mineral phases, as observed in the present study, exposure to acidic conditions will result in extensive leaching. In contrast, even in mildly oxidising conditions, U^{4+} will be readily oxidised to aqueous and soluble U^{6+} species across the whole pH range, including at high pH. This was exemplified in the current study by the oxidative dissolution of $CaZr_{0.80}U_{0.20}Ti_{2.00}O_7$ in HNO_3, which gave rise to greater U release than other less-oxidising acid solutions. At high pH, in 1M NaOH, the U release was an order of magnitude greater than the release of Ce in the counterpart sample.

The generic Pourbaix diagram (i.e. 25 °C, 1 bar) for Pu (Fig. 8c) most closely resembles that of Ce (Fig. 8a). The accessible oxidation states available to Pu within a zirconolite wasteform will be the same as those for Ce, i.e. Pu^{4+} and Pu^{3+}-stabilised perovskite (if present). Therefore, it is more likely that a Pu-containing zirconolite would behave like Ce than U under the leaching conditions applied here. Moreover, provided the perovskite content of a Pu-substituted zirconolite ceramic wasteform does not exceed trace levels, the leach resistance, even in aggressive acidic media, is expected to be very high and effectively preclude fissile material recovery. It should be noted, however, that Pu can exist in higher oxidation states, most notably PuO_2^{2+}, especially under highly oxidising, acidic conditions (Fig. 8c). For example, in nuclear fuel reprocessing performed in high-molarity HNO_3, Pu^{4+} is oxidised to the soluble plutonyl ion, $PuO_2^{2+}{}_{(aq)}$. Nevertheless, Pu is much less prone to oxidation into the more soluble +6 oxidation state than U and, therefore, less susceptible to the proposed oxidative dissolution mechanism. This is because the electrochemical cell potential of the U^{4+} to U^{6+} transition is lower than that of the corresponding reaction for Pu and thus occurs more readily. Therefore, even under highly oxidising acidic conditions, a single-phase Pu-zirconolite should be expected to exhibit a much lower Pu release than observed for U from a U-containing counterpart. In the present study, this equated to a release of ~1.7 % of the total U inventory.

In summary, we conclude that the susceptibility of zirconolite compositions to accelerated leaching is influenced by the leaching environment, the targeted zirconolite stoichiometry, and the choice of surrogate used. In particular, the potential for secondary phase ingrowth, which may segregate some portion of the fissile surrogate fraction, is considered to promote premature release for

Ce- and U-bearing zirconolite wasteforms. The accelerated leaching conditions imposed in these experiments do not pertain to disposal conditions, and hence these data cannot be considered representative of zirconolite wasteform leaching in groundwater. There is a clear need for further trials to underpin the dissolution behaviour of optimised zirconolite compositions under conditions representative of the geological disposal environment, to elucidate whether the effects observed in the present study also occur in multi-cation and -anion, near-neutral groundwater solutions, or whether other factors (e.g. complexation by carbonate ions, presence of colloids etc.) are likely to influence the overall dissolution mechanism.

METHODS

Materials synthesis

Zirconolite ceramics with nominal stoichiometry $CaZr_{0.80}Ce_{0.20}Ti_{2.00}O_7$ and $CaZr_{0.80}U_{0.20}Ti_{2.00}O_7$ were prepared from a mixture of component oxides: $CaTiO_3$ (Sigma Aldrich, 99.9% trace metals basis), ZrO_2 (Sigma Aldrich, 99.9% trace metals basis), TiO_2 (anatase, Sigma Aldrich, 99.9% trace metals basis), CeO_2 (Acros Organics, 99.9% trace metals basis) and UO_2 (ABSCO Ltd.). Materials were weighed according to target composition and placed into a 250 mL Y-stabilised ZrO_2 jar and milled at 500 rpm for approximately 40 min with ZrO_2 milling media, using a Fritsch P7 planetary mill. Isopropanol was added as a milling agent. The homogenised precursor slurries were then discharged and dried at 80 °C overnight to allow the evaporation of the excess solvent. Reclaimed batch materials were then calcined at 600 °C for 12 h (air atmosphere for $CaZr_{0.80}Ce_{0.20}Ti_{2.00}O_7$ and flowing Ar gas for $CaZr_{0.80}U_{0.20}Ti_{2.00}O_7$), before being packed into the walls of HIP canisters (grade 316 stainless steel) under uniaxial pressure to achieve maximum packing density. The can lids were then welded into place, before being placed under vacuum and evacuated until an internal can pressure of ~7 Pa was reached. The canisters were then heated under 300 °C until the vacuum recovered, before being crimped shut to ensure a hermetic seal. The cans were placed into the AIP-630 HIP unit and HIPed at 1300 °C, with a 100 MPa dwell pressure maintained for 4 h, using inert Ar gas as the densification medium. Processing of the radioactive ^{238}U containing $CaZr_{0.80}U_{0.20}Ti_{2.00}O_7$ sample was facilitated by the use of the active furnace isolation chamber (AFIC) plug-in component, protected under patent WO 2018/009782 A1[28,29]. The AFIC module is capable of processing U/Th-containing wasteform materials under hot isostatic conditions, preventing dispersal of radioactive material to the HIP pressure vessel in the event of a containment breach. The reformulated $Ca_{0.80}Zr_{0.90}Ce_{0.30}Ti_{1.60}Al_{0.40}O_7$ zirconolite composition was prepared by a conventional cold press and sinter method. Component oxides ($CaTiO_3$, ZrO_2, TiO_2, Al_2O_3 and CeO_2, as above) were weighed according to the desired composition and placed into a 125 mL ZrO_2-lined milling jar with 250 g of 3 mm ZrO_2 milling media, and 25 g isopropanol. The milling jar was placed into a Retsch PM100 Planetary Mill and homogenised at 500 rpm for 2 h. The powder slurry was recovered and dried to evaporate the excess solvent and pressed into the walls of a 25 mm stainless steel die under 100 MPa uniaxial pressure. Densified powder compacts were then placed into a tube furnace and sintered in air; the temperature was increased at a rate of 5 °C/min to 1250 °C, followed by 2 °C/min to 1350 °C with a dwell time of 4 h, before cooling to room temperature at a rate of 5 °C/min.

Materials characterisation

$CaZr_{0.80}Ce_{0.20}Ti_{2.00}O_7$ and $CaZr_{0.80}U_{0.20}Ti_{2.00}O_7$ compositions were sectioned from the HIP canister using a Buehler IsoMet 1000 low speed saw, with material from the bulk recovered for characterisation. All materials were crushed and sieved to recover material in the size fraction 75–150 µm. Powder X-ray diffraction (XRD) data were collected using a Bruker D2 Phaser (Cu Kα source: $\lambda = 1.5418$ Å) with a Ni filter, equipped with a Lynxeye position-sensitive detector. Data were acquired in the range $5^\circ \le 2\theta \le 80^\circ$ with a step size of 0.02° s^{-1}. Scanning electron microscopy (SEM) analyses were performed using either a Hitachi TM3030 (Figs. 4, Supplementary Fig. 1, 3 and 4) operating with a 15 kV accelerating voltage at a working distance of 8 mm or FEI Inspect 50 (Fig. 5) operating at 20 kV accelerating voltage and 10.6 mm working distance. Ce L_3 edge X-ray absorption near-edge structure (XANES) spectra were acquired in transmission mode at the Photon Factory Synchrotron beamline BL-27 (Tsukuba, Japan) using a conventional transmission configuration, with the ring operating at 2.5 GeV and 300 mA. Spectra were collected between 5590 eV and 5990 eV with the following energy steps (with a step rate 1 s^{-1}): 5 eV (5590–5690 eV), 0.5 eV (569 –5790), 1 eV (5790–5890 eV), 5 eV (5890–5990). U L_3 edge XANES was acquired at Diamond Light Source (Beamline B18 - Oxford, UK) using a fluorescence configuration. Incident radiation was scanned using a Si(111) monochromator and transmitted beam intensity was measuring using an ionisation chamber filled with a mixture of He and N_2 gas. Fluorescence emission was detected using a four-channel Si-drift detector. Ce L_3 and U L_3 edge XANES spectra were acquired alongside a selection of reference compounds: $CePO_4$, CeO_2, UTi_2O_6, $CrUO_4$ and $MgUO_4$, representing Ce and U in various oxidation states and coordination environment. XANES data reduction and analysis were performed using the Demeter suite[30]. A linear combination fit of Ce L_3 XANES was performed with respect to Ce reference compounds, to determine the relative speciation of Ce^{3+}/Ce^{4+}, using the Athena component of the Demeter package. The average oxidation state of U was calculated by linear regression of the U L_3 E_0 position (determined as the energy where the normalised edge step was equal to 0.5 i.e. $x\mu(E) = 0.5$), with respect to reference compounds of known oxidation state ($U^{4+}Ti_2O_6$, $CrU^{5+}O_4$, $MgU^{6+}O_4$). Compositions were prepared for XANES analysis by finely grinding reacted material with polyethylene glycol (PEG) and pressed in a 13 mm stainless steel die to a thickness equivalent to one absorption length.

Leaching methodology

Since the measured leaching efficiency could be strongly biased by the presence of an adherent fine fraction (<75 µm), prior to static leaching, particulates within the 75–150 µm size fraction were repeatedly washed in isopropanol solvent, as per the ASTM PCT-B protocol[31] and ultra-sonicated to suspend and remove fines. SEM analysis confirmed that the cleaning process had sufficiently removed any entrained fine particulates (Supplementary Fig. 5). Leach tests were performed using 0.5 g of material added to 10 mL of leachate within Teflon vessels. The surface area was determined geometrically and the resulting surface area to volume ratio was 600 m^{-1}. The leaching media investigated were 1M HNO_3 (Fisher, analytical reagent grade, 70%), 1M H_2SO_4 (Fluka, Puriss p.a. 95.0–97.0%), 1M HCl (Fisher, analytical reagent grade 37%), 1M NaOH (Merck, EMSURE pellets for analysis, 99–100%) and 8M HNO_3 (Fisher, analytical reagent grade, 70%). All experiments were performed in duplicate, with duplicate blanks (i.e. leaching media only), in a controlled temperature oven at 90 ± 2 °C for 7 days. At the termination of each experiment, an aliquot of each solution was removed from each vessel, filtered using a Whatman 0.22 µm nylon syringe filter, and diluted in 1% HNO_3. Elemental concentrations (mg L^{-1}) of constituent elements were analysed by Inductively Coupled Plasma Optical Emission Spectrometry (ICP-OES, Thermo Fisher 6000 iCAP Duo), using a six-point matrix-matched calibration with a 1% HNO_3 flush between samples. Concentrations measured in solution by ICP-OES were normalised to the nominal batch composition, thus allowing the batch leaching efficiency to be calculated as a percentage of the constituent element released from the pristine material into the leachate. The data were collated as such to compare the accelerated leaching properties of each zirconolite composition, with reference to the surrogate fissile fraction release to the aqueous phase in each instance. Accordingly, the normalised release of each element, reported as a percentage, was calculated from Eqs. 2 and 3.

$$m_{ij} = (C_{ij} \times V_{fj}) - \sum_{(k=1)}^{a} V_{bk} \times \frac{B_{ik}}{a} \quad (2)$$

where m_{ij} is equal to mass of element i released from the test sample j (in g); C_{ij} is equal to the concentration of element i measured in leaching solution from the test sample j (in g L^{-1}); V_{fj} is equal to the final volume of leachate in a test vessel containing the test sample j (in L); B_{ik} is equal to the concentration of element i measured in test blank k (in g); V_{bk} is equal to the final volume of solution in test blank k (in L); a is the number of blank solutions used for background solutions. This was then used to calculate the normalised elemental release as per Eq. 3:

$$NE_{\%} = \left(\frac{m_{ij}}{f_i \times m_j}\right) \times 100 \quad (3)$$

where $NE_{\%}$ is equal to normalised elemental release from sample j based on element i (in %); m_{ij} is as calculated from Eq. 2 (in g); f_i is the mass fraction of element i in test sample j; m_j is equal to the mass of test sample j (in g). The

reported values represent the average of duplicate samples. Geochemical modelling of the experimental data from the leaching solutions was performed with the geochemical speciation software PHREEQC, using the Lawrence Livermore National Laboratory thermodynamic database, LLNL-TDB[32]. These calculations are valid for temperatures in the range 0–300 °C. In order to quantify the degree of saturation of the solution in regards to the precipitation of some phases, the saturation index, SI, was calculated using Eq. 4.

$$SI = \log \frac{IAP}{K_S^0} \quad (4)$$

with *IAP* representing the ion activity product for the given phase dissolution reaction, and K_s^0 representing the standard solubility constant related to the phase.

DATA AVAILABILITY

The data that support these findings cannot be shared at this time, as the data also form part of an ongoing study.

Received: 12 January 2021; Accepted: 13 April 2021;
Published online: 20 May 2021

REFERENCES

1. Hyatt, N. C. Safe management of the UK separated plutonium inventory: a challenge of materials degradation. *npj Mater. Degrad.* **4**, 28 (2020).
2. Gatehouse, B. M., Grey, I. E., Hill, R. J. & Rossell, H. J. Zirconolite, $CaZr_xTi_{3-x}O_7$; Structure refinements for near-end-member compositions with x = 0.85 and 1.30. *Acta Cryst.* **B37**, 306–312 (1981).
3. Blackburn, L. R. et al. A systematic investigation of the phase assemblage and microstructure of the zirconolite $CaZr_{1-x}Ce_xTi_2O_7$ system. *J. Nucl. Mater.* **535**, 152137 (2020).
4. Gilbert, M. R. et al. Synthesis and characterisation of Pu-doped zirconolites - $(Ca_{1-x}Pu_x)Zr(Ti_{2-2x}Fe_{2x})O_7$. *IOP Conf. Ser. Mater. Sci. Eng.* **9**, 012007 (2010).
5. Ma, S. et al. Effects of ionic radius on phase evolution in Ln-Al co-doped $Ca_{1-x}Ln_xZrTi_{2-x}Al_xO_7$ (Ln = La, Nd, Gd, Ho, Yb) solid solutions. *Ceram. Int.* **44**, 15124–15132 (2018).
6. Begg, B. D., Day, R. A. & Brownscombe, A. Structural Effect of Pu Substitutions on the Zr-site in Zirconolite. in *Mat. Res. Soc. Symp. Proc.* **663**, 1–8 (2001).
7. Ewing, R. C., Weber, W. J. & Lian, J. nuclear waste disposal-pyrochlore ($A_2B_2O_7$): Nuclear waste form for the immobilization of plutonium and 'minor' actinides. *J. Appl. Phys.* **95**, 5949–5971 (2004).
8. Clinard, F. W. et al. Alpha decay self-irradiation damage in ^{238}Pu-substituted zirconolite. *J. Nucl. Mater.* **105**, 248–256 (1982).
9. Begg, B. D., Vance, E. R., Day, R. A., Hambley, M. & Conradson, S. D. Plutonium and neptunium incorporation in zirconolite. *Mater. Res. Soc. Symp. Proc.* **465**, 325–332 (1997).
10. Meng, C., Ding, X., Li, W., Zhao, J. & Yang, H. Phase structure evolution and chemical durability studies of Ce-doped zirconolite–pyrochlore synroc for radioactive waste storage. *J. Mater. Sci.* **51**, 5207–5215 (2016).
11. Cai, X., Teng, Y., Wu, L., Zhang, K. & Huang, Y. The synthesis and chemical durability of Nd-doped single-phase zirconolite solid solutions. *J. Nucl. Mater.* **479**, 455–460 (2016).
12. Strachan, D. M. et al. Radiation damage effects in candidate titanates for Pu disposition: Zirconolite. *J. Nucl. Mater.* **372**, 16–31 (2008).
13. Icenhower, J. P. et al. Dissolution kinetics of pyrochlore ceramics for the disposition of plutonium. *Am. Miner.* **91**, 39–53 (2006).
14. Smith, K. L., Lumpkin, G. R., Blackford, M. G., Day, R. A. & Hart, K. P. The durability of Synroc. *J. Nucl. Mater.* **190**, 287–294 (1992).
15. Vance, E. R. et al. Incorporation of uranium in Zirconolite ($CaZrTi_2O_7$). *J. Am. Ceram. Soc.* **85**, 1853–1859 (2002).
16. Zhang, Y. et al. Zirconolite-rich titanate ceramics for immobilisation of actinides - waste form/HIP can interactions and chemical durability. *J. Nucl. Mater.* **395**, 69–74 (2009).
17. Marples, J. A. C. The plutonium-zirconium phase diagram. *J. Less Common. Met.* **2**, 331–351 (1960).
18. Albiol, T., Serizawa, H. & Arai, Y. Studies in the PuO2-ZrO2 pseudo-binary phase diagram. *J. Nucl. Sci. Technol.* **3**, 834–837 (2002).
19. Vance, E. R. et al. In *Environmental Issues and Waste Management Technologies in the Ceramic and Nuclear Industries IX* .(eds. Vienna J. D. & Spearing D. R.) (Wiley, 2006).
20. Grey, I. E., Mumme, W. G., Ness, T. J., Roth, R. S. & Smith, K. L. Structural relations between weberite and zirconolite polytypes - Refinements of doped 3T and 4M $Ca_2Ta_2O_7$ and 3T $CaZrTi_2O_7$. *J. Solid State Chem.* **174**, 285–295 (2003).
21. Hubert, S., Heisbourg, G., Dacheux, N. & Moisy, P. Effect of inorganic ligands and hydrogen peroxide on ThO_2 dissolution. Behavour of $Th_{0.87}Pu_{0.13}O_2$ during leaching test. *Inorg. Chem.* **47**, 2064–2073 (2008).
22. Nesbitt, H. W. et al. Thermodynamic stability and kinetics of perovskite dissolution. *Nature* **289**, 358–362 (1981).
23. Myhra, S., Bishop, H. E., Rivière, J. C. & Stephenson, M. Hydrothermal dissolution of perovskite ($CaTiO_3$). *J. Mater. Sci.* **22**, 3217–3226 (1987).
24. Pham, D. K., Neall, F. B., Myhra, S., Smart, R. S. C. & Turner, P. S. Dissolution mechanisms of $CaTiO_3$ - solution analysis, surface analysis and electron microscope studies – Implications for Synroc. *Mat. Res. Soc. Symp. Proc.* **127**, 231–240 (1989).
25. Zhang, Z., Blackford, M. G., Lumpkin, G. R., Smith, K. L. & Vance, E. R. Aqueous dissolution of perovskite ($CaTiO_3$): effects of surface damage and [Ca^{2+}] in the leachant. *J. Mater. Res.* **20**, 2462–2473 (2005).
26. Clark, B. M., Sundaram, S. K. & Misture, S. T. Polymorphic transitions in cerium-substituted zirconolite ($CaZrTi_2O_7$). *Sci. Rep.* **7**, 2–10 (2017).
27. Blackburn, L. R., Walling, S. A. & Hyatt, N. C. et al. Synthesis and characterisation of $Ca_{1-x}Ce_xZrTi_{2-2x}Cr_{2x}O_7$: analogue zirconolite wasteform for the immobilisation of stockpiled UK plutonium. *J. Eur. Ceram. Soc.* **40**, 5909–5919 (2020).
28. Gardner, L. J., Walling, S. A. & Hyatt, N. C. Hot isostatic pressing: thermal treatment trials of inactive and radioactive simulant UK intermediate level waste. *IOP Conf. Ser. Mater. Sci. Eng.* **818**, 012009 (2020).
29. Hyatt, N. C. et al. The HADES Facility for High Activity Decommissioning Engineering & Science: part of the UK National Nuclear User Facility. *IOP Conf. Ser. Mater. Sci. Eng.* **818**, 012022 (2020).
30. Ravel, B. & Newville, M. ATHENA, ARTEMIS, HEPHAESTUS: Data analysis for X-ray absorption spectroscopy using IFEFFIT. *J. Synchrotron Radiat.* **12**, 537–541 (2021).
31. ASTM International. Standard test methods for determining chemical durability of nuclear, hazardous, and mixed waste glasses and multiphase glass ceramics: The Product Consistency Test (PCT). https://doi.org/10.1520/C1285-14.2.
32. Parkhurst, D. L. & Appelo, C. A. J. Description of input and examples for PHREEQC Version 3—A Computer Program for Speciation, Batch-Reaction, One-Dimensional Transport, and Inverse Geochemical Calculations. Chapter 43 of Section A, in Groundwater Book 6, Modeling Techniques, Techniques and Methods 6-A43 (1999). https://pubs.usgs.gov/tm/06/a43/pdf/tm6-A43.pdf.
33. Brookins, D. G. Eh-pH diagrams for geochemistry. *Geochim. Cosmochim. Acta* 53, (1989).

ACKNOWLEDGEMENTS

We acknowledge financial support from the Nuclear Decommissioning Authority (NDA) and EPSRC under grant numbers EP/S01019X/1, EP/N017870/1 and EP/R511754/1. CLC is grateful to EPSRC for the award of an Early Career Research Fellowship under grant number EP/N017374/1. This research utilised the HADES/MIDAS facility at the University of Sheffield established with financial support from EPSRC and BEIS, under grant EP/T011424/1. Collection of the Ce L_3 edge XAS data was performed under the approval of the Photon Factory Advisory Committee (Proposal No. 2019G586); the support of Yoshihiro Okamoto (Japanese Atomic Energy Agency) and Noriko Usami (The High Energy Accelerator Research Organisation - Kō Enerugī Kasokuki Kenkyū Kikō) during the experiment is gratefully acknowledged. We acknowledge Diamond Light Source for time on Beamline B18 under Proposal SP17243 and wish to thank G. Cibin for assistance with data acquisition.

AUTHOR CONTRIBUTIONS

Lewis Blackburn —conceptualisation, data collection, formal analysis, original draft preparation. Rachel Crawford— data collection, formal analysis, reviewing and editing. Samuel Walling — data collection, formal analysis, reviewing and editing. Laura Gardner — data collection, formal analysis, reviewing and editing. Max Cole — data collection, formal analysis, reviewing and editing. Shi-Kuan Sun— data collection, formal analysis, reviewing and editing. Clémence Gausse — data collection, formal analysis, reviewing and editing. Amber Mason — data collection, formal analysis, reviewing and editing. Martin Stennett —supervision, formal analysis, reviewing and editing. Ewan Maddrell— supervision, formal analysis, reviewing and editing. Neil Hyatt — funding acquisition, supervision, formal analysis, reviewing and editing. Claire Corkhill —funding acquisition, supervision, formal analysis, reviewing and editing.

COMPETING INTERESTS

The authors declare no competing financial or non-financial Interests.

ADDITIONAL INFORMATION

Supplementary information The online version contains supplementary material available at https://doi.org/10.1038/s41529-021-00171-8.

Correspondence and requests for materials should be addressed to C.L.C.

Reprints and permission information is available at http://www.nature.com/reprints

Publisher's note Springer Nature remains neutral with regard to jurisdictional claims in published maps and institutional affiliations.